

# Macroscopic equivalence for microscopic motion in a turbulence driven three-dimensional self-assembly reactor

T.A.G. Hageman and P.A. Löthman

*KIST Europe, Campus E7.1, 66125 Saarbrücken, Germany  
University of Twente, PO Box 217, 7500 AE Enschede, The Netherlands and  
Saarland University, 66123 Saarbrücken, Germany*

M. Dirnberger

*Max Planck institute for Informatics, Campus E1.4, 66123 Saarbrücken, Germany and  
Saarland University, 66123 Saarbrücken, Germany*

M. Elwenspoek

*University of Twente, PO Box 217, 7500 AE Enschede, The Netherlands*

A. Manz

*KIST Europe, Campus E7.1, 66125 Saarbrücken, Germany and  
Saarland University, 66123 Saarbrücken, Germany*

L. Abelmann\*

*KIST Europe, Campus E7.1, 66125 Saarbrücken, Germany and  
University of Twente, PO Box 217, 7500 AE Enschede, The Netherlands*

(Dated: 8 August 2017)

We built and characterised a macroscopic self-assembly reactor that agitates magnetic, centimeter-sized particles with a turbulent water flow. By scaling up the self-assembly processes to the centimeter-scale, the characteristic time constant scale also drastically increases. This makes the system a physical simulator of microscopic self-assembly, where the interaction of inserted particles are easily observable. Trajectory analysis of single particles reveals their velocity to be a Maxwell-Boltzmann distribution and it shows that their average squared displacement over time can be modelled by a confined random walk model, demonstrating a high level of similarity to Brownian motion. The interaction of two particles has been modelled and verified experimentally by observing the distance between two particles over time. The disturbing energy (analogue to temperature) that was obtained experimentally increases with sphere size, and differs by an order of magnitude between single-sphere and two-sphere systems (approximately 80  $\mu\text{J}$  versus 6.5  $\mu\text{J}$ , respectively).

## I. INTRODUCTION

Self-assembly is the process in which a disorganised system assembles in a specific product without external interference. The final properties of the assembly are determined by the properties of the individual parts. Self-assembly is used extensively by nature; for example, in crystal growth, protein folding, the assembly of molecules into larger compounds, and the creation of complex organs such as the human brain.

Self-assembly is a prospective candidate for use in areas where conventional production and assembly methods are problematic. Although it is not limited to specific dimensions [1], self-assembly is especially applicable to small scales [2]; for example, because conventional machining tools for three-dimensional construction are limited to larger feature sizes, while photo-lithography processes are two-dimensional in nature. Mastrangeli *et al.*'s [3] review gives an excellent summary of this area, ranging from nanosized DNA origami [4] to magnetically folded milli-scale structures [5].

Arguably, one of the most promising applications will arise in the semiconductor industry. As a result of the continuous

downscaling of fabrication processes, non-volatile data storage systems will at some point run into its limit to store and process bits of information using only a few atoms [6]. To achieve higher data densities, it is necessary to move to the third dimension. The first steps in this direction have been taken by stacking wafers [7] or layers [8]. However, the stacking approach is not suitable to achieve truly three-dimensional structures, in which both the resolution and extent of the features is identical in all directions [9]. We believe that the most promising production method is three-dimensional self-assembly.

Not only is three-dimensional self-assembly a prospective candidate for highly repetitive memory structures, it will also open a path for more complex electronics, such as processors. For instance, Gracias *et al.* [10] have designed millimeter-sized polyhedra with integrated electronics. By self-assembling these into crystals, functional electrical circuits have been demonstrated on a centimeter-scale. Scaling down the building blocks is a crucial step towards scalability of the system as a whole.

It has been demonstrated that microscopic spherical particles can form regular structures upto centimeter-sized dimensions [11]. By tuning the particle properties and/or the driving force of self-assembly, one can control the size and dimensions of the resulting structures [12, 13].

---

\* Email: l.abelmann@kist-europe.de

Although major progress has been made in three-dimensional microscopic self-assembly, observing the dynamic behaviour during the assembly process remains a challenge due to the small size and time constants involved. Several approaches have been explored to model and simulate these processes [14–16]. However, these approaches rely on exhaustive Monte-Carlo simulations, scaling unfavourably with the number of particles involved.

Magnetic forces have been used extensively as driving forces in self-assembly on all scales, together with various sources of agitating energy.

When exposed to an external magnetic field, it has been demonstrated that nanoscopic magnetic rods form bundles ([17]) or multimers when driven by ultrasound ([8]). Although paramagnetic spheres form chains, they will form ribbon structures (connected, parallel chains) for chains exceeding 30 particles ([18, 19]) and flower-like patterns result when magnetic and non-magnetic beads are mixed with ferrofluids ([20]). In the absence of an external magnetic field, a theoretical study of off-centered magnetic dipoles in spherical particles ([21]) shows that lateral displacement of the dipoles results in structures that are more compact than chains. On millimeter-scales, magnetic forces and vibrations have been used to quickly and efficiently assemble particles with correct orientation on a template ([22, 23]). Also on centimeter-scales, magnetic forces have been used to form particles rather than structures, such as the spontaneously folding elastomeric sheets with embedded electronics; as demonstrated in ([24]). Lash *et al.* ([25]) showed that polystyrene beads self-assemble into HCP packed structures by solvent evaporation. Larger polystyrene particles ( $>18\ \mu\text{m}$ ) required additional disturbing energy (ultrasonic energy) as a disturbing energy source to self-assemble. Macroscopic self-assembly processes on a centimeter scale are dominated by two-dimensional structures, where mechanical shaking is the most widely used source of disturbing energy.

Hacohen *et al.* [26] demonstrated DNA-inspired patterned bricks with embedded magnets, self-assembling into a programmed structure, but report gravity bias. Stambaugh *et al.* [27] reported self-assembled 2D structures of centimeter-sized spherical particles with internal magnets that were shaken vertically, and observed different resulting structures that were based on particle concentration and magnet shape. Ilievsky *et al.* [28] demonstrated self-assembly of centimeter-sized magnetic cubes into chains in a turbulent flow by submerging them in a rotating reactor filled with water, this way introducing eddy flows as a disturbing energy. They also introduced the concept of effective temperature, describing the motion of particles as if Brownian by nature. Even though the assembly process is three-dimensional, the resulting structures are limited to a single dimension and the dynamics involved are not studied.

To build upon this work, we introduce an experimental setup, which is designated “macroscopic self-assembly reactor”, as a simulator for microscopic self-assembly. In this reactor, we study the motion and interaction of centimeter-sized objects. Particles are subject to a downward gravitational force and a drag force that is created by an upward water flow. We chose the particle density to balance these forces,

causing them to appear weightless. Following Ilievski [28], we use a turbulent water flow as an agitating source, simulating the Brownian motion on a microscopic scale. We employ permanent magnets, resulting in attraction forces between the particles.

By increasing particle size from micrometers to centimetres, not only the ease of observation but also the characteristic time constants increase decidedly. This makes the self-assembly process visible using conventional cameras. As a result of scaling up the system, the environment also changes; laminar flows become turbulent while inertia effects become dominant. At the same time, Brownian motion becomes negligible. Therefore, it is crucial to study to what extent the macroscopic system is a good simulator for microscopic environments, which is the main topic of this publication.

### I.1. Organisation of this paper

We characterise the motion and dynamics of particles in a macroscopic self-assembly reactor. By observing the trajectories of a single particle in the reactor, we quantify the similarity between Brownian motion of said dynamics. By observing the interaction of two particles in the reactor, we can characterise the most fundamental building block of the self-assembly process, which is the interaction of magnetic spheres in a turbulent environment. Section II gives a theoretical description of Brownian motion in a confined environment, and provides a model of two-particle interaction based on Maxwell-Boltzmann (M-B) statistics. Section III introduces the reactor and magnetic particles in detail. Subsequently, in Section IV we successfully analyse the extent to which the results of single- and two-particle experiments match our expectations based on the models.

## II. THEORY

Brownian motion is the apparent motion of microscopic particles suspended in a fluid or gas, resulting from collisions with their surrounding molecules, and it can be characterised by a three-dimensional random walk.

### II.1. Diffusion

A random walk has an average square displacement that increases linearly as time increases. We can define a diffusion constant  $D$  [ $\text{m}^2\text{s}^{-1}$ ], which in a system with three degrees of freedom links average displacement  $\langle x^2 \rangle$  [ $\text{m}^2$ ] to time  $t$  [s] according to

$$\langle x^2 \rangle = 6Dt. \quad (1)$$

This model holds only if the average distance travelled is much smaller than the size of the container in which the particles move. In our experiment this is not the case and, therefore, container geometry needs to be taken into account.

To account for the confined space, we first consider a particle performing a random walk along a single dimension. The particle displacement with respect to its starting location after  $t$  seconds is normally distributed with variance  $\sigma_x^2 = 2Dt$ . Hence, the average squared displacement  $\langle x^2 \rangle$  is equal to the variance of the distribution. The probability of the particle being outside of the confined space is zero. To account for this effect, we replace the normal distribution by a truncated normal distribution. If the truncation is symmetrical on both tails of the normal distribution,  $x_t$  [m], then the truncated distribution is given by

$$n_t(x, \sigma, x_t) = \begin{cases} \frac{n(x, \sigma)}{N(x_t, \sigma) - N(-x_t, \sigma)} & -x_t \leq x \leq x_t \\ 0 & \text{otherwise,} \end{cases} \quad (2)$$

where  $n(x, \sigma)$  is the normal distribution and  $N(x, \sigma)$  is the cumulative normal distribution. The average squared displacement of a confined particle is the variance of this distribution:

$$\langle x^2 \rangle = \sigma^2 \left( 1 - \frac{x_t n(x_t, \sigma)}{N(x_t, \sigma) - \frac{1}{2}} \right). \quad (3)$$

For  $x_t/\sigma \gg 1$ , the particle does not yet experience the confinement. In this situation  $n(x_t, \sigma) \approx 0$  and  $\langle x^2 \rangle = \sigma^2$ . For  $x_t/\sigma \ll 1$  the chance of finding the particle in the container is uniformly distributed ( $n_t = 1/2x_t$ ), and  $\langle x^2 \rangle$  saturates at  $x_t^2/3$ .

When moving to three dimensions, the average squared displacement of the separate dimensions can be simply summed because they are orthogonal.

The diffusion coefficient can only be determined if there has been a sufficient amount of collisions. In between the collisions, particles have constant velocity and direction. Due to the stochastic nature of the collision events, the velocity autocorrelation decays exponentially with time constant [29, 30]

$$\tau_v = \frac{m^*}{f}, \quad (4)$$

where  $f$  [ $\text{kg s}^{-1}$ ] is the drag coefficient and  $m^*$  [kg] is the effective mass.

The situation for  $t \ll \tau_v$  is referred to as the ballistic regime. Here, the average squared distance travelled  $\langle x^2 \rangle$  is quadratic rather than linear in time. The transition from the (quadratic) ballistic regime to the (linear) diffusion regime (eq. 1) is modelled phenomenologically by:

$$\sigma^2 = 6D \frac{t^2}{t + \tau_v}. \quad (5)$$

Note that both the effective mass  $m^*$  and the drag coefficient  $f$  depend on the environment. The effective mass takes into account the fact that when the particle is accelerated, the surrounding water mass is also accelerated. For incompressible fluids with either zero viscosity or infinite viscosity (Stokes

flow), the added mass is 50 % of the mass of the water displaced by the sphere [31]. For turbulent flow, both experiment [32] as well as numerical simulations [33, 34] show that the added mass is also to a good approximation 50 %, irrespective of the Reynolds number or acceleration. There are reports that the added mass might be bigger in cases where the sphere is traveling through its own wake [35], which is rare in our experimental setup. Therefore, we have suggested a simple estimate of the added mass,

$$m^* = m + \frac{2}{3} \pi r^3 \rho_{\text{fluid}}, \quad (6)$$

for a particle with radius  $r$  [m] and mass  $m$  [kg] surrounded by a fluid with density  $\rho_{\text{fluid}}$  [ $\text{kg m}^{-3}$ ].

## II.2. Velocity distribution

Li *et al.* [36] have experimentally proven that the velocity of particles performing a Brownian motion is M-B distributed. This distribution of velocity  $v$  [ $\text{m s}^{-1}$ ] is determined by its mode  $v_p$ ,

$$p(v) = \frac{4v^2}{\sqrt{\pi} v_p^3} e^{-\left(\frac{v}{v_p}\right)^2}. \quad (7)$$

At the mode, the distribution reaches its maximum; thus  $v_p$  is the most probable velocity. For completeness, we note that the average squared velocity is  $\langle v^2 \rangle = \frac{3}{2} v_p^2$ .

## II.3. Drag coefficient

Brownian motion is primarily studied on the microscopic scale, where the Reynolds number is much smaller than unity. In this case, the drag force is linear in velocity and the relevant drag coefficient  $f$  is equal to the Stokes drag coefficient. However, on a macroscopic scale, we deal with turbulent flow and a high Reynolds number, where the drag force  $F_d$  [N] is quadratic in velocity,

$$F_d = \frac{1}{2} \rho_{\text{fluid}} C_d A v^2, \quad (8)$$

where  $C_d$  is the drag coefficient and  $A$  [ $\text{m}^2$ ] is the cross sectional area of the object in the direction of motion.

In our experiment, the particles are continuously ‘‘falling’’ through the upward water flow. This upward flow is set to the terminal velocity  $v_t$  of the particles, so that they levitate in front of the camera. Assuming that the changes in the velocity of the particle caused by turbulence are much smaller than the terminal velocity, we can obtain an effective drag coefficient by linearising around the terminal velocity

$$f = \left. \frac{dF_d}{dv} \right|_{v=v_t} = \rho_{\text{fluid}} C_d A v_t. \quad (9)$$

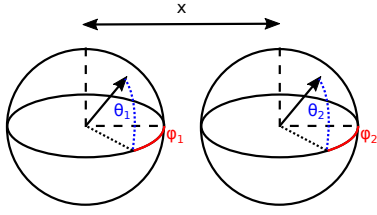


FIG. 1: The interaction between two spheres modelled by magnetic dipoles at distance  $x$  with orientation vector  $\theta = [\theta_1 \ \phi_1 \ \theta_2 \ \phi_2]$ .

#### II.4. Disturbing energy

On the microscale, the diffusion coefficient and velocity distribution of particles in the fluid can be linked to the temperature. This concept can be extrapolated to macroscale systems where disorder is achieved by shaking rather than by temperature. In that case, one speaks about effective temperature [28, 37], which is usually significantly higher than the environmental temperature. Since shaking can be highly directional, we prefer to characterize the shaking action by energy ( $kT$  [J]) rather than temperature to avoid confusion.

Starting from the velocity distribution (eq. 7), and considering that  $\langle v^2 \rangle = 3kT/m$  for three-dimensional random walks, the most probable velocity is related to the kinetic energy through:

$$kT = \frac{1}{2} m^* v_p^2. \quad (10)$$

The Einstein relation also relates the diffusion constant and viscous drag coefficient of a particle to the thermal energy  $kT$ :

$$kT = fD. \quad (11)$$

If particles in a self-assembly reactor behave according to Brownian motion, both relation (10) and (11) can be used to obtain the disturbing energy and should give identical results.

In addition to measuring the disturbing energy  $kT$  from Brownian motion, we can also estimate it from the interaction between two attracting magnetic objects. In this situation, we use the fact that the probability of the system being in a state is governed by M-B statistics. Consider a system of two spherical magnetic particles in a confined space (Figure 1). The chance that the distance of those particles measured from center-to-center is smaller than  $x_0$  is:

$$\begin{aligned} p(x \leq x_0) &= \frac{1}{Z} \int_d^{x_0} \int_{\theta} g_r(x) e^{-\frac{E_m(\theta, x)}{kT}} d\theta dx \quad (12) \\ Z &= \int_d^D \int_{\theta} g_r(x) e^{-\frac{E_m(\theta, x)}{kT}} d\theta dx \\ \theta &= [\theta_1 \ \phi_1 \ \theta_2 \ \phi_2]. \end{aligned}$$

Here  $g_r(x)$  is the probability density function of a sphere pair with distance  $x$  between their centers, unaffected by magnetic forces, which models the influence of the geometry of the reactor.

The distance between the cylindrical magnets is at all times at least a factor of four of the magnet height  $h$  ( $h \leq d/4$ ). At this point, we approximate their magnetic field as well as their magnetic moments by point dipoles. This approximation is accurate within 1.3 % for our magnet geometry. In that case, the magnetic energy of particle 1 with magnetic moment  $\mathbf{m}(\theta_1, \phi_1)$  [A m<sup>2</sup>] in a field  $\mathbf{B}(\theta_2, \phi_2, x)$  [T] generated by particle 2 reduces to

$$E_m(\theta, x) = -\mathbf{m}(\theta_1, \phi_1) \cdot \mathbf{B}(\theta_2, \phi_2, x). \quad (13)$$

Equation (12) can be approximated numerically by a Monte-Carlo approach in which a large number of random combinations of sphere locations and orientations are selected, yielding different values for  $E_m$ . The geometry factor  $g_r$  is approximated by repeated random sampling of two point locations in a confined geometry and then gathering statistics about their distance.

### III. MATERIALS AND METHODS

#### III.1. Reactor

The experimental setup consists of a transparent cylinder with an inner diameter of 17.3(1) cm containing the particles of interest (Figure 2). Gravity is counteracted by pumping water from the bottom to the top via four 4.0(1) cm diameter inlet holes using a MAXI.2 40T pump (PSH pools). The water exiting the cylinder is collected in an open container connected to the pump inlet. The water flow entering the pump is monitored using an altometer (IFS 4000, Krohne Messtechnik GmbH).

Meshes spaced at 17 cm prevent the particles from moving outside the field of view of cameras placed around the reactor. The dynamics of the particle-fluid system are determined by the particle density and geometry, as well as water flow speed.

#### III.2. Particles

The particles used in the experiments are 3D-printed polymeric (ABS) spheres with a diameter of 1.67(1) to 2.02(2) cm and a corresponding density of 1.33(2) to 1.25(4) g cm<sup>-3</sup> (larger particles have lower density). The core of the spheres consist of cylindrical, axially magnetised NdFeB magnets with a length of 3.80(5) mm and a diameter of 3.80(5) mm (Supermagnete, grade N42, Webcraft GmbH). The dipole moment (50.8(1) mA m<sup>2</sup>) was determined by measuring the force between two magnets using a balance.

The drag coefficient of the particles was estimated from their terminal drop velocity. For this, particles with a range of densities but identical diameter of 1.85 cm were released at the top of a 2 m high cylinder filled with water. Once an equilibrium between drag- and gravitational force had been established (approximately 0.5 m after release), the velocity of the particles was measured with a video camera over a distance of 1.0 m. Figure 3 shows the measured relation between drag force and terminal velocity. From fitting equation 8, we

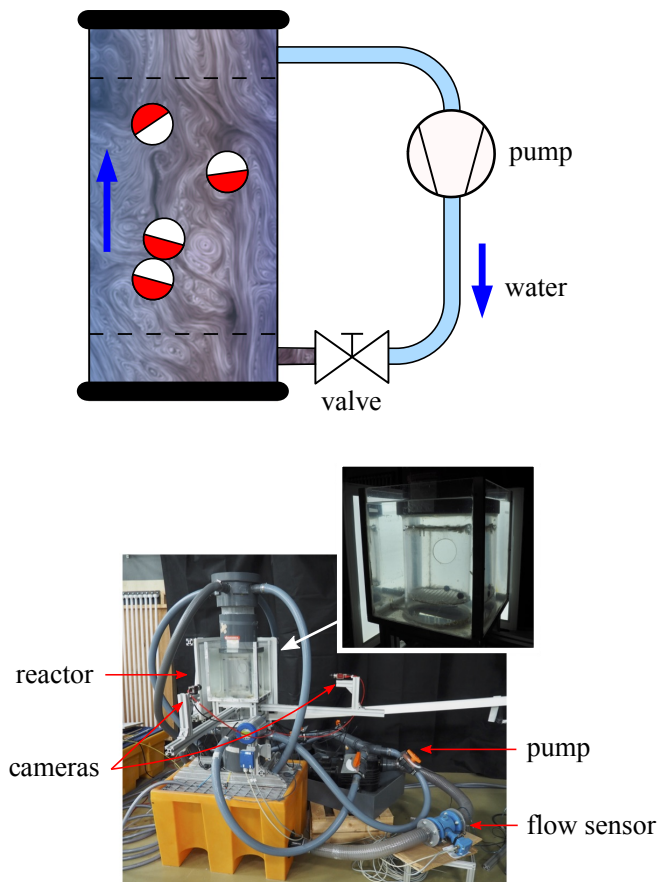


FIG. 2: Schematic (top) and experimental (bottom) setup of the macroscopic self-assembly reactor. Water is pumped from the bottom to the top of the reactor, counteracting gravity and supplying energy to the particles via turbulent flow. Meshes prevent the particles from moving outside of the field of view of cameras placed around the reactor.

obtain  $\frac{1}{2}\rho_{\text{fluid}}C_dA = 78(3) \text{ g m}^{-1}$ . Assuming the density of water to be  $1000 \text{ kg m}^{-3}$ , we obtain  $C_d=0.58(2)$ . Spheres of this diameter and velocity in water have a Reynolds number of approximately 5500. At this value, Brown *et al.* [38] predict  $C_d=0.39$ , which is substantially lower. The reason for the discrepancy is unknown to us. The measured drag coefficient is used in the remainder of this paper.

### III.3. Reconstruction

Two calibrated, synchronised cameras (Mako G-131, Allied Vision) were placed around the reactor at an angle of approximately  $90^\circ$  and they recorded datasets at 30 fps at a resolution of  $640 \times 512$ . The reactor is surrounded by a square, water-filled aquarium to prevent refraction due to its cylindrical nature. Backlight panels were used to enhance contrast. Single spheres were observed for 15 min and two spheres for 30 min. Offline, the location of the spheres was automatically detected using a custom written MATLAB script. A method based on the direct linear transform algorithm [39] was used

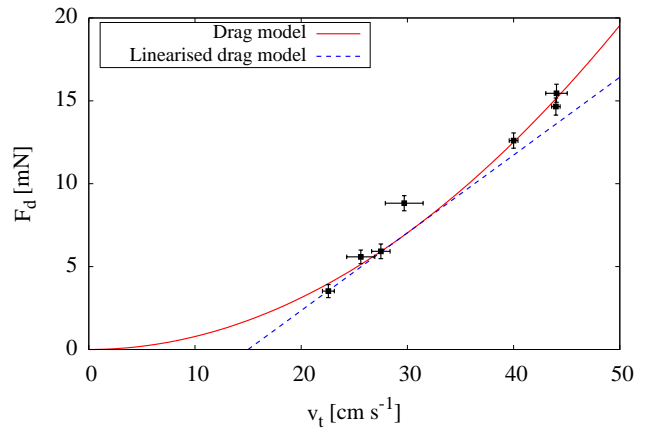


FIG. 3: Calculated drag force versus measured terminal velocity for spheres with equal diameter but varying densities. The effective drag coefficient is obtained by linearisation around the terminal velocity (eq. 9), illustrated by the blue dashed line for  $v_t=30 \text{ cm s}^{-1}$ .

for 3D reconstruction, giving an average reconstruction error of 0.16 cm. Trajectories closer than 1.5 cm to the meshes were discarded to rule out the significant effect of the altered hydrodynamic interaction at these interfaces. The velocity vector of the particle is obtained by  $\mathbf{v} = \Delta \mathbf{x} f_{\text{cam}}$ , the product of the particle displacement between two frames, and the camera frame rate.

## IV. RESULTS

### IV.1. Single particles

Figure 4 shows a set of reconstructed trajectories of a 1.85 cm sphere in the reactor. Each trajectory starts and ends when exiting and entering the areas within 1.5 cm of the meshes, and is indicated by a different color.

Figure 5 shows the velocity calculated from these trajectories. The histogram is obtained from the absolute velocity (10600 data points) of a 1.80 cm sphere. A M-B distribution was fitted to the data by minimising the maximum distance  $E_{\text{max}}$  between the cumulative empirical and cumulative M-B distribution, yielding fitting parameter  $v_p$ . A Kolmogorov-Smirnoff (K-S) test was used to quantify the quality of fit and to obtain a significance level  $Q$  to disprove the null hypothesis that the two distributions are the same. [40] With a  $E_{\text{max}}$  of 0.0073 and a  $Q$  of 0.70, we have good reason to assume that the velocity is MB-distributed.

Figure 6 displays the resulting  $v_p$  for spheres of various diameters, for which we find a range from  $15.92$  to  $17.54 \text{ cm s}^{-1}$ . The fit to the M-B distribution has a  $Q$ -value above 0.05 for five out of the seven measurements. Even though the data suggests a slight decrease of velocity with increasing sphere size, the particle velocity fits very well to a model assuming constant velocity, with an average of  $16.6(2) \text{ cm s}^{-1}$ . This analysis was carried out using a chi-square fitting routine, yielding the reduced  $\chi^2$  error metric (ideally being around 1) and the corresponding  $Q$ -value (the

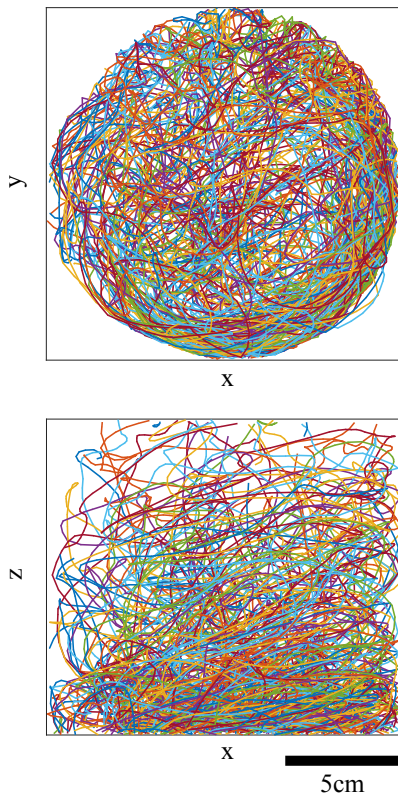


FIG. 4: Top (upper) and side (bottom) view of the reconstructed trajectories of a single sphere (diameter 1.85 cm) moving through the reactor. Coordinates less than 1.5 cm close to the top- and bottom meshes are removed to rule out significant influence of the meshes. In this way, the single trajectory is cut into many smaller ones, which are each assigned a different color. See Supplementary Material at [URL will be inserted by publisher] for a three dimensional representation of the data.

probability that a  $\chi^2$  equal or greater than the observed value is caused by chance). [40] The reduced  $\chi^2$  of this fit is close to unity (0.68) with a very high  $Q$ -value of 0.67.

Figure 7 shows the normalised distribution of the particle at several  $z$ -slices across the reactor. It can be seen that the particle has a preference for the bottom area, especially near the reactor walls of the positive  $x$ -coordinate. We believe that this phenomenon is caused by a non-uniform flow pattern of water that results from the specific valve settings.

The average squared displacement was calculated from the longest trajectories; that is, those with a minimum duration of 2.0 s. Figure 8 shows the resulting curve for a sphere with a diameter of 1.90 cm. The curve shows a quadratic regime below 0.3 s, shortly entering an approximate linear regime before slowly converging to a horizontal asymptote.

The movement of the sphere is in the quadratic, or ballistic, regime when the measurement time is shorter than the average time between directional changes (“collisions”),  $\tau_v$ . Using measured values for the drag coefficient and effective mass in equation 4, we obtain values for  $\tau_v$  ranging from 134 to 149(10) ms. The saturation measured for longer observations is caused by the confined geometry of the reactor and it will change as the reactor is changed in shape and size.

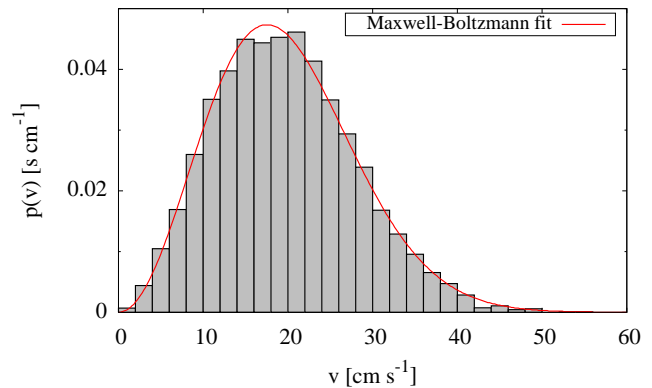


FIG. 5: Maxwell-Boltzmann (M-B) distribution fitted to the measured velocity distribution of a particle with a diameter of 1.80 cm. The Kolmogorov-Smirnov (K-S) test quantifies a maximum distance between the theoretical and experimental cumulative distributions of 0.0073 with a  $Q$  value of 0.70, indicating a high probability that the velocity is indeed M-B distributed.

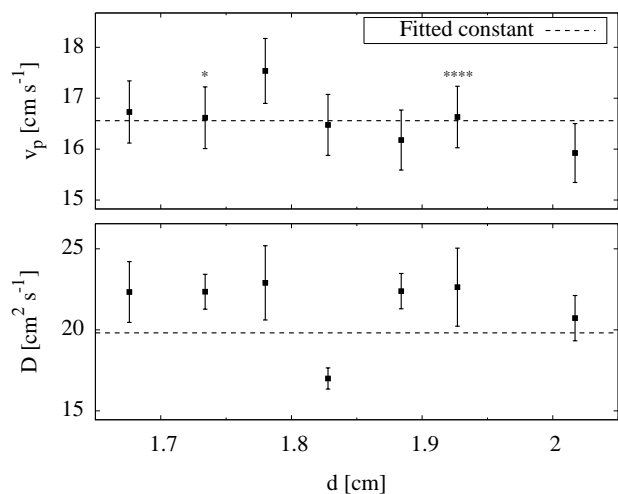


FIG. 6: **Top:** Mode of the M-B distribution obtained by fitting to the measured velocity distribution of particles of various diameters (reduced  $\chi^2 = 0.68$ ,  $Q = 0.67$ ). Stars indicate the quality of fit ( $Q$ -value) of the K-S test (\* < 0.05, \*\*\*\* < 0.0001). **Bottom:** Diffusion coefficient obtained by fitting the diffusion model to the average square displacement (reduced  $\chi^2 = 5.85$ ,  $Q = 4 \cdot 10^{-6}$ ).

The model described by equations 3 and 5 was fitted to the measurements, yielding values for diffusion coefficient  $D$  and average reactor size  $x_1$ .

We have to take into account that the model has its limitations. First of all it is based on a symmetrical truncated normal distribution. This would require the particle to always start in the center of the reactor. In contrast, all of the measured trajectories start at a random place at the top or bottom of the reactor due to the method that we used to obtain separate trajectories.

Secondly, the cylindrical geometry of the reactor is not in-

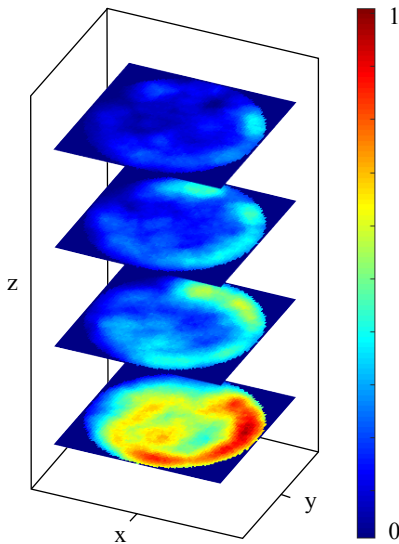


FIG. 7: Normalised probability distribution of a single sphere (diameter 1.85 cm) in the reactor, displayed in slices along the reactor tube. The particle has a clear preference for the bottom region as well as the edge regions. Quantised, the particle has a chance of 62 %, 48 % and 26 % to be in, respectively, the right (positive  $x$ -coordinate), back (positive  $y$ -coordinate) and top (positive  $z$ -coordinate) halves of the reactor.

cluded in the model. These two issues mainly affect the estimation of the reactor size.

Finally, the ballistic regime was phenomenologically modelled without physical background. This region, which has a high weight factor during fitting the model to the data (due to the small error bars in the data), can result in a significant fitting error.

Given that only the latter aspect could give errors in the estimation of  $D$ , we consider the obtained values for  $D$  to be quite reasonable, with values between 17 and 23  $\text{cm}^2 \text{s}^{-1}$  (see figure 6). The average diffusion coefficient for all of the measured diameters is 20(1)  $\text{cm}^2 \text{s}^{-1}$ . Judging from the graph, there seems to be no reason to assume that the diffusion coefficient has a strong dependence on sphere diameter. It should be noted, however, that this assumption leads to a very high reduced  $\chi^2$  (5.85) and low quality of fit  $Q$  ( $4 \cdot 10^{-6}$ ). However, due to the previously mentioned model inaccuracies, we think that we may have underestimated the errors in the estimation of  $D$ .

#### IV.2. Two-sphere results

From the two-sphere experiments, the distance  $x$  between the particles was tracked over time. Figure 9 shows the cumulative probability of sphere distance  $p(x \leq x_0)$  for spheres of various diameters. Spheres with smaller diameters have a lower magnetic energy in connected state and, therefore, a higher probability of being connected. In other words,  $p(x \leq d)$  becomes larger for smaller  $d$ . All of our measurements follow a similar profile: they consist of a curved regime

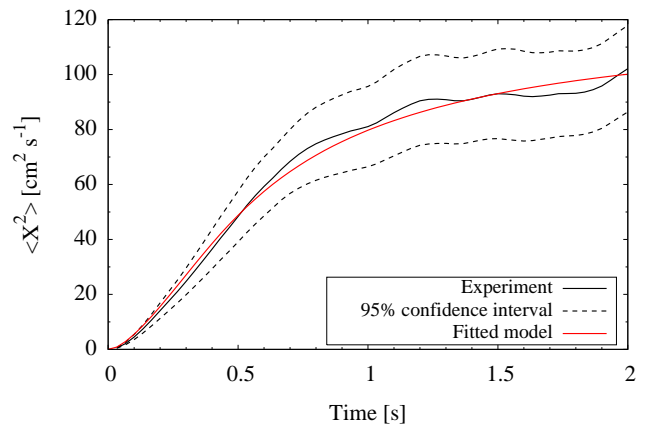


FIG. 8: Average squared displacement as a function of time for a sphere with diameter 1.90 cm, calculated from 65 trajectories. The model fits within the 95 % confidence interval.

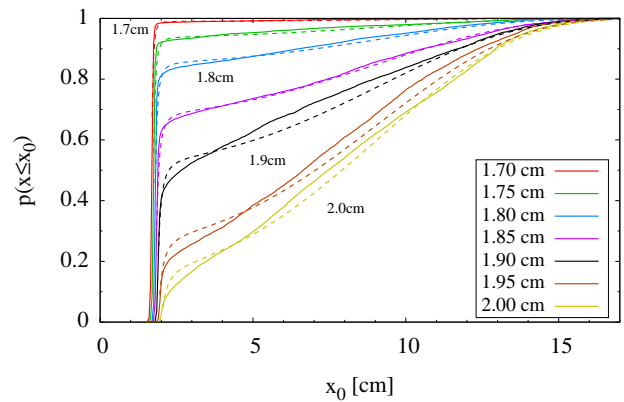


FIG. 9: Measured probability (cumulative) of the distance between the centers of two magnetic spheres ( $x$ ) for various sphere diameters. A model based on M-B statistics captures the shapes of the curves with a maximum error of 5 % of the full range. As the spheres decrease in size, they are more likely to be in a connected state.

for  $x \leq 3$  cm followed by an approximately linear region for  $x > 3$  cm. The linear regime indicates that magnetic forces are no longer significant for particle interaction. For  $x > 13$  cm there is a saturation effect caused by the reactor geometry. The model of equation 12 has been fitted to the curves by minimising the maximum distance between the curves (based on the Kolmogorov-Smirnoff method [40]). Although this is not an exact fit, it manages to capture the shape with a maximum error of 5 % of the full range.

#### IV.3. Disturbing energy

The experiments provide three methods for the characterisation of the equivalent thermal energy of the system. Numerical values for the kinetic energy were calculated from the

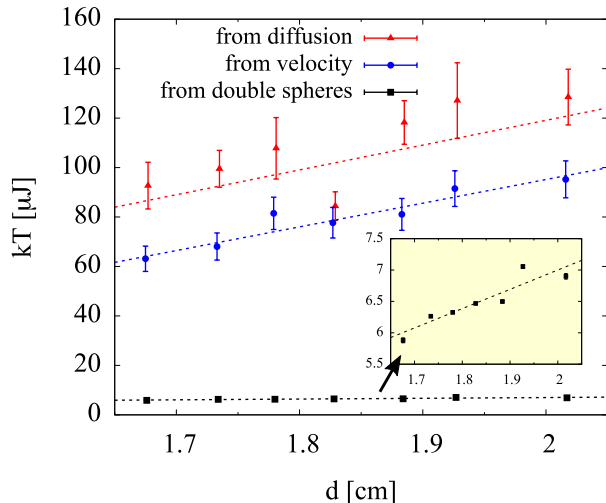


FIG. 10: Disturbing energy of the turbulent field calculated from the diffusion coefficient, the velocity distribution and double sphere experiments. The disturbing energy estimated from the single sphere experiments (diffusion, velocity) are approximately a factor 10 higher than that estimated from double sphere experiments. The dashed lines are guides to the eye. There is an increase in energy with an increase in sphere diameter, which is proportional with the increase in mass and friction coefficient.

measured velocity and added mass according to equation 10. The measured diffusion coefficient and drag coefficient at the set water flow speed (equation 9) were used to calculate the energy using the Einstein relation (equation 11). Additionally, two-particle experiments provide numerical values for the equivalent energy as a result of fitting equation 12 to the measured data, as depicted in figure 9.

The resulting values for all of the spheres are summarised in figure 10. A first observation is that the results obtained via single sphere experiments (velocity, diffusion) are in the same order of magnitude, and differ approximately  $20 \mu\text{J}$ . They span a range from approximately 60 to  $120 \mu\text{J}$ . These values are, however, more than a factor of ten higher than the results obtained via the two sphere experiments, which range from approximately 6 to  $7 \mu\text{J}$ . The possible origin for this discrepancy is discussed in the following section.

In all cases, the energy increases as the sphere size increases, by approximately 17%, 41%, and 46% for, respectively, two-sphere experiments, diffusion, and velocity. As we concluded previously, the diffusion coefficient and average sphere velocity do not depend on the sphere size (figure 6). The increase of energy is caused by an increase in mass and friction coefficient, and both are dependent on sphere radius.

## V. DISCUSSION

From the trajectory analysis of single particles, we were able to determine that their velocity distribution closely follows a M-B distribution. Additionally, we have seen that the

average squared displacement as a function of time follows a shape that was predicted by a confined random walk model. These conclusions strongly support the hypothesis that particles in the reactor perform a random walk.

When increasing the particle size, the observed disturbing energy  $kT$  also increases. However, there is no observable increase in velocity or diffusion coefficient. For the energy calculated via velocity and diffusion, this means that this increase in energy is caused by an increase in, respectively, effective particle mass and drag coefficient. The corresponding curves, as shown in figure 10, are very similar due to the fact that the particle mass and drag force are coupled. With an increase in particle radius, both the mass and surface area are increased. The increase in energy occurs without physically changing the nature of the disturbing energy; that is, the speed and turbulence of the water flow is unaltered. This means that the amount of energy that is transferred from the environment to the particle is dependent on the particle geometry.

An explanation for this effect might be found in the wavelength dependence of the turbulence. Turbulence is introduced as a large wavelength disturbance at the bottom of the cylinder, after which it propagates upwards in an energy cascade that transfers the energy to smaller wavelengths. This process is dissipative (Richardson cascade [41]). The resulting energy spectrum drops off at increasing wave numbers. [42] Therefore, we can assume that the disturbing energy as experienced by the particles is not, like in Brownian motion, characterised by a flat spatial frequency spectrum (white noise) but instead drops off at shorter wavelengths. So, effectively, the bandwidth of the energy transfer increases for larger particles.

The assumption of a dissipative energy cascade could also explain why the energy obtained from two-sphere experiments is lower compared to single sphere experiments. While all of the spatial frequency components in the turbulent flow drive an object around the system in a random walk, wavelengths in order of the particle diameter contribute most effectively to separation of connected particles. The disturbing energy dropping with decreasing wavelength would explain why the disturbing energy estimated from the two particle experiment is smaller than that obtained from the random walk.

It is perhaps in the spatial frequency spectrum where the analogy between turbulent flow and true Brownian motion breaks down. Therefore, we will need to characterise the effective energy of the system separately for particles of different size. Special care needs to be taken for large clusters of particles because they are effectively a large particle and, therefore, subject to a higher energy portion. At the same time, particle-particle interaction is subject to a lesser amount of disturbing energy. Consequently, such systems will have a bias towards the occurrence of smaller particle clusters.

## VI. OUTLOOK

Successful self-assembly is characterised by the ability of the system to end up in a desired end-state, generally the global energy minimum. This will require an interplay in assembling and disturbing forces which assist the system by removing itself from local energy minima. The experimen-



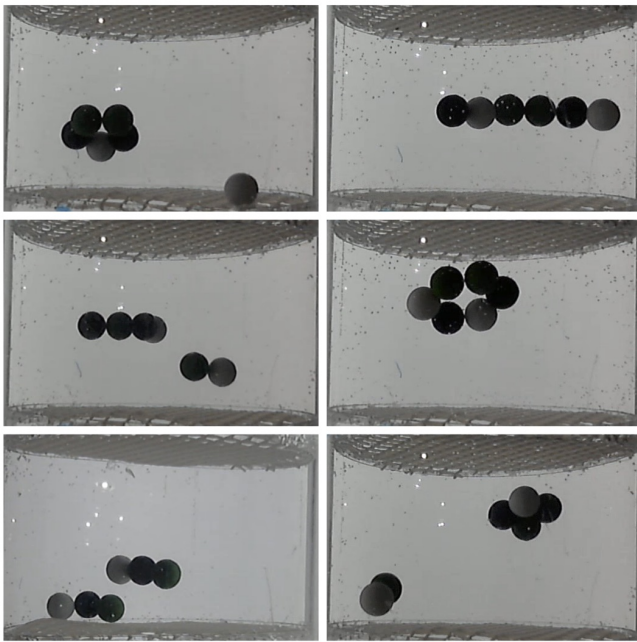


FIG. 11: Multi-particle systems show to explore the energy landscape, ending up in both local and global energy minima. See Supplementary Material at [URL will be inserted by publisher] for a video of the processes taking place.

tal results have proven that particles in the reactor show a Brownian-like motion and that the disturbing turbulent field is able to separate otherwise connected particles. This gives confidence that multi-particle systems will be able to explore the energy landscape and that the results have significance for similar processes taking place on the microscale.

To demonstrate the possibilities of using this experimental setup for further studies, we loaded the reactor with six spheres with embedded magnets. Figure 11 shows several stills of a video in which the spheres form different structures, thereby exploring the energy landscape. The highest energy state is found when all of the spheres are disconnected. The energy of the system decreases with the number of connections made, so a six sphere chain structure (top right) has a lower energy than two three-sphere structures (bottom left). One more bond can be created by forming a six-sphere ring (center right). For structures with more than four spheres, the ring is the minimum energy state [43]. Indeed, three-sphere rings are hardly ever observed. By long term observation, one could measure the relative occurrence of the different structures and check if they agree with Boltzmann statistics.

## VII. CONCLUSIONS

We have constructed an experimental setup that allows us to study the (dis)connection dynamics of centimeter-scale objects by analysing the interaction of magnetic attraction forces and disturbing turbulent forces. This “macroscopic self-assembly reactor” serves as a physical simulator of self-assembly processes on the microscale and nanoscale, allowing

easy observation by drastically increasing both the length and time scales.

Trajectory analysis of single spherical particles shows that they perform a random walk, which analogous to Brownian motion. Spheres with diameters ranging from 1.7 to 2.0 cm have a range of velocities that are M-B distributed. The most probable velocity (mode) is independent on sphere size and has a value of  $16.6(2) \text{ cm s}^{-1}$ . The average square displacement over time, or the ‘diffusion profile,’ fits to a confined random walk model. The diffusion coefficient appears to be independent of sphere size, with an average value of  $20(1) \text{ cm}^2 \text{ s}^{-1}$ . Although statistical analysis disproves this statement, we believe that the measurement error has been underestimated.

The particle distribution is non-uniform over the reactor. The particle is, for instance, three times as often in the bottom half of the reaction compared to the top half. Although this non-uniform distribution does not affect the Brownian motion behaviour, it virtually reduces the reactor size.

In two-particles systems, we observe self-assembly dynamics; that is, the particles occasionally connect and disconnect. The cumulative distribution of the distance between the centers of the particles fits with a maximum error of 5 % of the full range of the distribution to a model based on M-B statistics.

The disturbing energy (analogue to temperature) of the reactor was estimated from the velocity distribution and diffusion (single particle experiments), as well as from the dynamic interaction of two-particle systems. The estimates of the disturbing energy determined from single sphere experiments are in the same order of magnitude. However, the disturbing energy obtained from two-sphere experiments is at least one order of magnitude lower (approximately  $6.5 \mu\text{J}$  compared to  $80 \mu\text{J}$ ). From this we can conclude that for self-assembly studies, the disturbing energy of the system cannot be calibrated from single sphere experiments alone.

The disturbing energy increases with increasing sphere diameter, from 1.7 to 2.0 cm. For the single sphere experiment, this increase is more prominent (41 % via diffusion analysis, 46 % via velocity analysis) than for the two-sphere experiment (17 %). We reason that the energy transfer from the turbulent environment to the particles is dependent on particle size and geometry.

In addition to the two-sphere experiment, periodic connection and disconnection events have also been observed for a six-sphere system, forming ring- and line-based structures. This demonstrates that the reactor can be successfully applied to study self-assembly processes at convenient length and time scales, and it may be a good simulator for microscopic environments.

## ACKNOWLEDGEMENTS

The authors would like to thank Remco Sanders for constructing the self-assembly reactor and Léon Woldering for initial work on the project. Additionally, we thank John Sader for introducing the concept of added mass and Marc Pichel for his participation in scientific discussions and general sup-

port. We also recognise the valuable contribution of Nikodem Bienia, Donghoon Kim, Gayoung Kim, Yannick Klein and Minyoung Kim to the scientific work. Finally, we would

like to thank Bronkhorst BV for providing the flow meter, and Eckard Breuers for kindly providing nets of various dimensions for our experiments.

- 
- [1] G. M. Whitesides and B. Grzybowski, *Science* **295**, 2418 (2002).
- [2] M. Elwenspoek, L. Abelmann, E. Berenschot, J. van Honschoten, H. Jansen, and N. Tas, *J. Micromech. Microeng.* **20**, 064001 (2010).
- [3] M. Mastrangeli, S. Abbasi, C. Varel, C. van Hoof, J. P. Celis, and K. F. Böhringer, *Journal of Micromechanics and Microengineering* **19**, 1 (2009).
- [4] P. W. K. Rothmund, *Nature* **440**, 297 (2006).
- [5] E. Iwase and I. Shimoyama, *Journal of Microelectromechanical Systems* **14**, 1265 (2005).
- [6] R. Bennewitz, J. N. Crain, A. Kirakosian, J. L. Lin, J. L. McChesney, D. Y. Petrovykh, and F. J. Himpel, *Nanotechnol.* **13**, 499 (2002).
- [7] M. Dellutri, P. Pulici, D. Guarnaccia, P. Stoppino, G. Vanalli, T. Lessio, F. Vassallo, R. Di Stefano, G. Labriola, A. Tenerello, F. Lo Iacono, and G. Campardo, *Thermal, Mechanical and Multi-Physics Simulation and Experiments in Micro-Electronics and Micro-Systems. Proceedings of EuroSimE 2006 (IEEE Cat. No.06EX1341)*, 5 pp. (2006).
- [8] H. Tanaka, M. Kido, K. Yahashi, M. Oomura, R. Katsumata, M. Kito, Y. Fukuzumi, M. Sato, Y. Nagata, Y. Matsuoka, Y. Iwata, H. Aochi, and A. Nitayama, *Digest of Technical Papers - Symposium on VLSI Technology*, 14 (2007).
- [9] L. Abelmann, N. Tas, E. Berenschot, and M. Elwenspoek, *Micromachines* **1**, 1 (2010).
- [10] D. H. Gracias, J. Tien, T. L. Breen, C. Hsu, and G. M. Whitesides, *Science* **289**, 1170 (2000).
- [11] A. Philipse, *J. Mater. Sci. Lett.* **8**, 1371 (1989).
- [12] V. N. Manoharan, M. T. Elsesser, and D. J. D. Pine, *Science* **301**, 483 (2003).
- [13] M. Rycenga, J. M. McLellan, and Y. Xia, *Advanced Materials* **20**, 2416 (2008).
- [14] Z. Zhang, A. Keys, T. Chen, and S. Glotzer, *Langmuir* **21**, 11547 (2005).
- [15] J. Grant, R. Jack, and S. Whitelam, *Journal of Chemical Physics* **135** (2011), 10.1063/1.3662140.
- [16] S. Whitelam and R. Jack, *Annual Review of Physical Chemistry* **66**, 143 (2015).
- [17] J. Love, A. Urbach, M. Prentiss, and G. Whitesides, *J. Am. Chem. Soc.* **125**, 12696 (2003).
- [18] A. Darras, J. Fiscina, M. Pakpour, N. Vandewalle, and G. Lumay, *The European Physical Journal E* **39**, 47 (2016).
- [19] R. Messina and I. Stankovic, *Physica A: Statistical Mechanics and its Applications* **466**, 10 (2017).
- [20] R. Erb, H. Son, B. Samanta, V. Rotello, and B. Yellen, *Nature* **457**, 999 (2009).
- [21] A. Yener and S. Klapp, *Soft Matter* **12**, 2066 (2016).
- [22] S. Shetye, I. Eskinazi, and D. Arnold, *IEEE Transactions on Magnetism* **44**, 4293 (2008).
- [23] S. Shetye, I. Eskinazi, and D. Arnold, *Journal of Microelectromechanical Systems* **19**, 599 (2010).
- [24] M. Boncheva, S. A. Andreev, L. Mahadevan, A. Winkleman, D. R. Reichman, M. G. Prentiss, S. Whitesides, and G. M. Whitesides, *Proceedings of the National Academy of Sciences* **102**, 3924 (2005).
- [25] M. Lash, M. Fedorchak, S. Little, and J. McCarthy, *Langmuir* **31**, 898 (2015).
- [26] A. Hachohen, I. Hanniel, Y. Nikulshin, S. Wolfus, A. Abu-Horowitz, and I. Bachelet, *Scientific Reports* **5** (2015), 10.1038/srep12257.
- [27] J. Stambaugh, D. Lathrop, E. Ott, and W. Losert, *Physical Review E - Statistical, Nonlinear, and Soft Matter Physics* **68**, 026207/1 (2003).
- [28] F. Ilievski, M. Mani, G. Whitesides, and M. Brenner, *Phys. Rev. E Stat. Nonlinear Soft Matter Phys.* **83**, (2011).
- [29] P. Langevin, *C. R. Acad. Sci. (Paris)* **146**, 530 (1908).
- [30] D. Lemons and A. Gythiel, *American Journal of Physics* **65**, 1079 (1997).
- [31] L. Landau and E. M. Lifshitz, *Fluid Mechanics* (PERGAMON PRESS, 1987).
- [32] J. Pantaleone and J. Messer, *American Journal of Physics* **79**, 1202 (2011).
- [33] E. Chang and M. Maxey, *Journal of Fluid Mechanics* **277**, 347 (1994).
- [34] E. Chang and M. Maxey, *Journal of Fluid Mechanics* **303**, 133 (1995).
- [35] F. Odar and W. Hamilton, *Journal of Fluid Mechanics* **18**, 302 (1964).
- [36] T. Li, S. Kheifets, D. Medellin, and M. G. Raizen, *Science* **328**, 1673 (2010).
- [37] S. Wang and P. Wolynes, *Journal of Chemical Physics* **135** (2011), 10.1063/1.3624753.
- [38] P. P. Brown and D. F. Lawler, *J. Environ. Eng.* **129**, 222 (2003).
- [39] R. I. Hartley and A. Zisserman, *Multiple View Geometry in Computer Vision*, 2nd ed. (Cambridge University Press, ISBN: 0521540518, 2004).
- [40] W. H. Press, S. A. Teukolsky, W. T. Vetterling, and B. P. Flannery, *Numerical Recipes in C (2nd Ed.): The Art of Scientific Computing* (Cambridge University Press, New York, NY, USA, 1992).
- [41] L. Richardson, *Weather prediction by numerical process* (Cambridge University Press, 1922).
- [42] A. Kolmogorov, *C. R. Acad. Sci. URSS* **30** (1941).
- [43] R. Messina, L. Khalil, and I. Stankovic, *Physical Review E - Statistical, Nonlinear, and Soft Matter Physics* **89** (2014), 10.1103/PhysRevE.89.011202.